ADVANCED FUNCTIONAL MATERIALS
www.afm-journal.de

Robust Systemic and Mucosal Immune Responses to Coxsackievirus B3 Elicited by Spider Silk Protein Based Nanovaccines via Subcutaneous Immunization

Xingmei Qi, Guoqiang Wei, Yanan Li, Sidong Xiong,* and Gefei Chen**

Coxsackievirus B3 (CVB3) is a member of the enterovirus genus and linked to several diseases, including myocarditis, which can progress to dilated cardiomyopathy. Despite ongoing preclinical efforts, no clinically approved vaccines against CVB3 are currently available, highlighting the urgent need for effective prophylactic solutions. In this study, a nanovaccine platform based on spider minor ampullate silk protein (MiSp) is introduced. This platform utilizes protein nanoparticles engineered from chimeric proteins that incorporate CVB3 antigenic peptides into customized MiSp, subsequently loaded with all-trans retinoic acid (RA). These functional nanovaccines are capable of eliciting both mucosal and systemic immune responses following subcutaneous administration and demonstrate significant protective effects against CVB3 infection in mice. This study signifies an approach in peptide-based parenteral vaccine strategies, utilizing engineered MiSp nanoparticles combined with RA. This methodology represents a promising pathway for preventing enterovirus infections by leveraging the unique immunomodulatory properties of spidroins and RA to combat these pathogens effectively.

1. Introduction

Vaccines play a pivotal role in public health for mitigating the spread of infectious diseases. Traditional vaccines, employing inactivated or live attenuated pathogens, have significantly contributed to the control of infectious diseases by stimulating adaptive immunity.[1–3] Despite their effectiveness, these vaccines pose safety concerns, including the potential to cause diseases they aim to prevent or to introduce harmful contaminants, leading to adverse effects.[4,5] In response, subunit vaccines, which contain only purified antigens or antigenic components of the pathogen, have emerged as a safer alternative due to their reduced risk of side effects.[4,6] However, the limited immunogenicity often results in suboptimal protection, necessitating the use of adjuvants or carrier materials to enhance vaccine efficacy.[6] Given that the primary route of entry for many infectious agents is through mucosal surfaces, the generation of mucosal antibodies, particularly immunoglobulin A (IgA), is crucial for intercepting pathogens at these entry points. Parenteral subunit vaccines typically struggle to elicit a mucosal immune response due to a mechanism that limits the access of peripherally stimulated lymphocytes to mucosal sites.[2] Moreover, while traditional vaccination approaches, including intramuscular, subcutaneous, or intradermal injections, are effective at provoking systemic immune responses, they generally are not able to induce robust mucosal immunity. Oral vaccines have been proposed to induce intestinal immunity, but their effectiveness is often compromised by the challenging gut environment and the lack of appropriate mucosal adjuvants. Several studies have shown that administering all-trans retinoic acid (RA), a vitamin A metabolite, can enhance the mucosal homing capabilities of T and B cells, thereby augmenting intestinal immune responses.[7–11] However, RA's limited solubility in water and the potential for immune tolerance with high doses present formulation challenges for parenteral vaccines.[8,10] In order to circumvent this, a parenteral vaccine strategy that enabled the induction of both systemic and mucosal immune response was achieved by co-delivery of RA with antigen by adjuvant.[7,10,11] Considering the general safety and efficacy profiles, developing a subunit vaccine formulation that enabled the induction of both systemic and mucosal immune responses is necessary.

X. Qi, G. Wei, S. Xiong
The Jiangsu Key Laboratory of Infection and Immunity
Institutes of Biology and Medical Sciences
Soochow University
Suzhou 215123, China
E-mail: xmqi@suda.edu.cn; sdxiong@suda.edu.cn
Y. Li
Department of Neurosurgery
Changhai Hospital
Naval Medical University
Shanghai 200433, China
G. Chen
Department of Biosciences and Nutrition
Karolinska Institutet
Huddinge 14157, Sweden
E-mail: gefei.chen@ki.se
G. Chen
Department of Cell and Molecular Biology
Uppsala University
Uppsala 75105, Sweden
The ORCID identification number(s) for the author(s) of this article can be found under https://doi.org/10.1002/adfm.202407568

DOI: 10.1002/adfm.202407568

Coxsackievirus B3 (CVB3), a member of the enterovirus genus within the Picornaviridae family, is a non-enveloped, single-stranded positive-sense RNA virus. Its infection spectrum is broad, ranging from mild flu-like symptoms to severe conditions that impact the heart, pancreas, and nervous system. Notably, CVB3 can cause viral myocarditis, a condition that may progress to dilated cardiomyopathy and ultimately require heart transplantation.[12–14] Beyond myocarditis, CVB3 has been linked to a variety of other diseases, including meningitis,[15,16] pancreatitis,[17] hand-foot-and-mouth disease,[18,19] and even the onset of type 1 diabetes.[19–23] Despite ongoing preclinical efforts,[24] no clinically approved vaccines against CVB3 are currently available, underscoring the urgent need for effective prophylactic measures. In recent years, nanoparticle-based systems have been developed as delivering platforms for drugs or vaccines.[25–29] Among these systems, spider silk proteins (spidroins) have attracted the interest due to their excellent properties such as inherent biocompatibility and biodegradability, the induction of no or negligible immune response and allow for solvent-free preparation and steam sterilization.[30–35] These features make spidroins an attractive candidate for vaccine delivery development, offering a promising avenue for the creation of safe and effective vaccine delivery system against challenging pathogens like CVB3.

This study explores a vaccination approach by integrating specific CVB3 antigenic peptides (epitopes) into engineered spider minor ampullate silk proteins (MiSp), combined with RA encapsulation. The complex nanovaccines can induce robust mucosal and systemic immune responses after subcutaneous injection and provide significant protective effects against CVB3 infections in mice. This study marks the initiation of a peptide-based parenteral vaccine strategy that employs engineered spidroin nanoparticles coated with RA, representing a promising avenue for the prevention of enterovirus infections.

2. Results

2.1. Characterization and Biosafety of CVB3 Nanovaccines

The capsid protein of CVB3 is a complex assembly composed of four capsid proteins, with the VP1 protein standing out as a pivotal antigenic target for the development of subunit vaccines. This prominence is due to its array of immunogenic epitopes that are capable of eliciting both T-cell and B-cell responses, along with its notable antibody neutralization potential.[36–39] To enhance the elicitation of mucosal immunity via subcutaneous injection, we strategically selected two epitopes from the VP1 protein to form the basis of our nanovaccine design. These include a B-cell epitope ($VP1^B$, positions 1–15: GPVEDAITAAIGRVA) and a T-cell epitope ($VP1^T$, positions 153–172: PDKVDSYVWQTSTNPSVFWT), both of which were pinpointed through the utilization of synthetic overlapping peptides in a series of in vitro and in vivo assays.[37,40] The chosen B-cell epitope is particularly effective in provoking CVB3-specific serum responses, whereas the selected T-cell epitope is instrumental in stimulating the production of interferon-gamma (IFN-γ), predominantly fostering a targeted immune defense against CVB3 infection. These two VP1 peptides were fused genetically to a customized spidroin NM, which is able to assemble into nanoparticles,[41] with a cathepsin S substrate linker (PMGLP) in between, respectively. Here, N is the N-terminal domain of *Araneus ventricosus* MiSp and M is part of the repetitive region. Based on this strategy, two chimeric proteins, NM-$VP1^B$ and NM-$VP1^T$ were generated (Figure S1a,b, Supporting Information). These chimeric proteins were expressed in *Escherichia coli* and induced to form nanoparticles through a salting-out process using potassium phosphate (Figure S1c,d, Supporting Information).[41–43] Interestingly, both types of nanoparticles were spherical and exhibited similar sizes under scanning electron microscopy (SEM), with diameters of 321 ± 1.5 nm for NM-$VP1^B$ and 293 ± 4.3 nm for NM-$VP1^T$ (**Figure 1**a,b). Additionally, the zeta potentials of these chimeric nanoparticles, a measure of their surface charge and stability in suspension, were closely matched at −23.8 ± 0.5 mV for NM-$VP1^B$ and −24.3 ± 1.8 mV for NM-$VP1^T$, as determined by dynamic light scattering (DLS) (Figure 1b; and Table S1, Supporting Information). This consistency in size and zeta potential underscores the reproducibility and precision of the chimeric nanoparticle formation process, highlighting its potential for uniform vaccine delivery platforms. To enhance the potential for boosting mucosal immunity through subcutaneous injection, these nanoparticles were further loaded with RA, named RA@NM-$VP1^B$ and RA@NM-$VP1^T$, respectively. The successful loading of RA was confirmed through absorbance measurements at 297 nm and observed color changes (Figure S1e,f, Supporting Information). These modifications resulted in an increase in average nanoparticle size and a reduction in zeta potential, with RA@ NM-$VP1^B$ showing a size of 442.3 ± 15.4 nm and a charge of −36.9 ± 0.6 mV and RA@NM-$VP1^T$ exhibiting a size of 439.7 ± 7.1 nm and a surface charge of −42 ± 0.5 mV (Figure 1b). And the RA loaded nanoparticles were still uniform and spherical (Figure 1a). Given that high concentrations of RA can activate retinoic acid receptor (RAR) and retinoid X receptor (RXR) nuclear receptors, leading to IL-10 mediated immunosuppression, and low concentrations might not sufficiently stimulate antigen-presenting cells (APCs),[10,27] the RA concentration in the nanoparticles was carefully optimized. By evaluating the maturation (CD86 expression) and IL-10 secretion levels of bone marrow-derived dendritic cells (BMDCs) exposed to different RA loadings (0.5, 0.75, and 1.0% of the nanoparticle mass), the optimal RA loading amount was finely tuned to ≈0.75% for further studies (Figure 1c,d). With aiming for both T-cell and B-cell responses, we created and investigated the nanovaccines by mixing equal amounts of NM-$VP1^B$ and NM-$VP1^T$ nanoparticles, resulting in the formulations NM-$VP1^{T/B}$ and RA@NM-$VP1^{T/B}$. The mix of RA@NM-$VP1^B$ and RA@NM-$VP1^T$ demonstrated a sustained release of RA at different pHs (Figure 1e), providing supportive evidence for its effectiveness in in vivo immunization scenarios.

The biocompatibility and safety profile of the nanoparticles were further assessed through a series of evaluations. RAW264.7 and BMDC cells were exposed to varying concentrations of the nanoparticles (100–1000 μg mL^{-1}), and cell viability was assessed using the CCK-8 cell proliferation assay. After 24, 48, or 72 h of exposure, no significant impact on cell viability was detected across the range of nanoparticle concentrations when compared to the control group (PBS), as evidenced by a qualitative comparison of cell density (Figure 1f,g). Furthermore, the

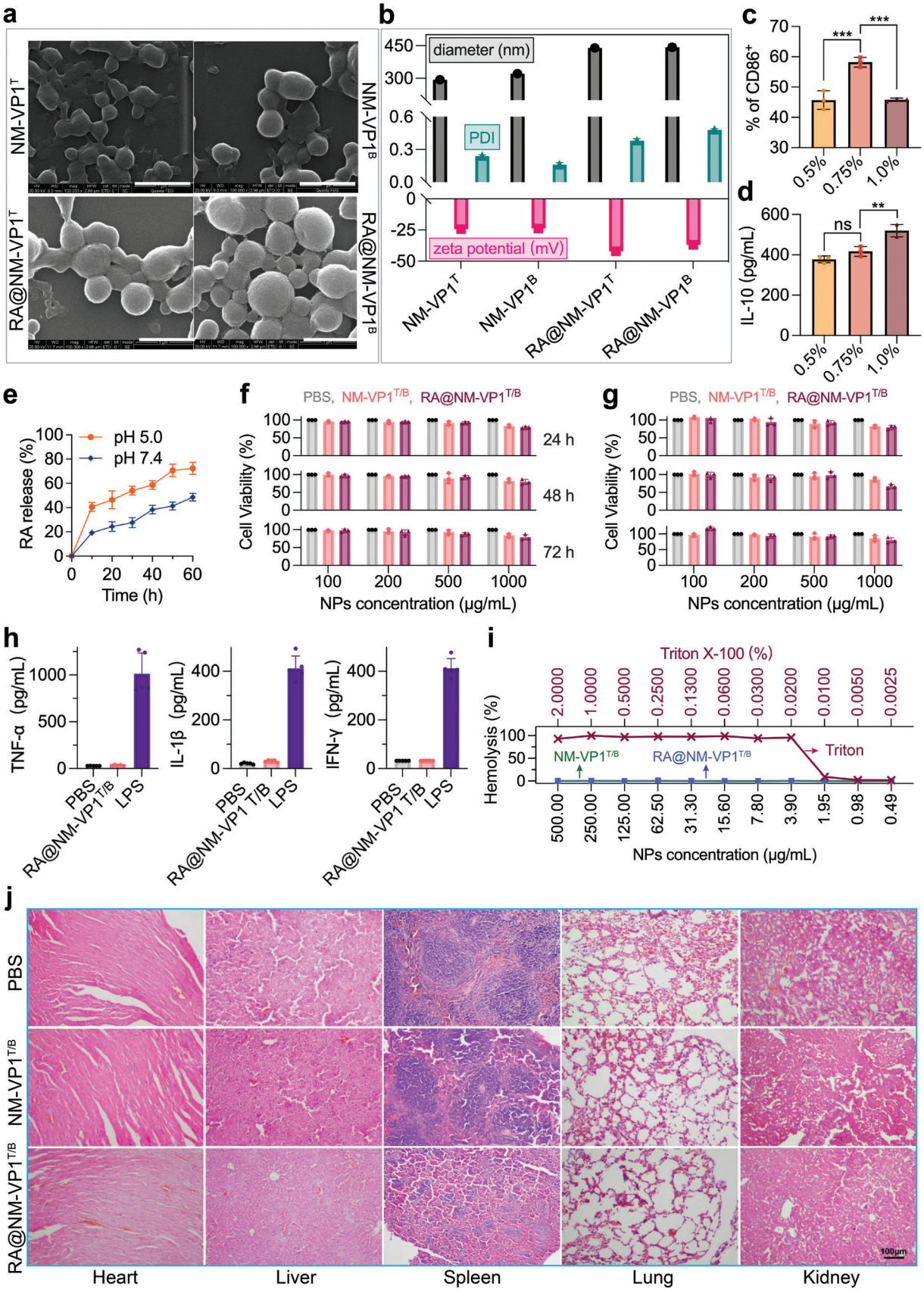

levels of interleukins (IL-1β), tumor necrosis factor-alpha (TNF-α), and interferon-gamma (IFN-γ) in the serum of mice immunized with RA@NM-VP1$^{T/B}$ were evaluated and no severe systemic inflammation was observed (Figure 1h). Additionally, the hemocompatibility of the nanoparticles was investigated through hemolytic assays. Different concentrations of nanoparticle were incubated with red blood cells (RBCs) for 30 min, and the absorbance of hemoglobin released from lysed RBCs was measured at 570 nm. The results showed that NM-VP1$^{T/B}$ and RA@NM-VP1$^{T/B}$ nanoparticles exhibited no hemolytic behavior at the highest concentration tested (Figure 1i), affirming their compatibility with blood components. Notably, a positive control demonstrated significant hemolytic activity, highlighting the benign nature of the nanoparticle in comparison (Figure 1i). Furthermore, histopathological analysis was conducted on major organs, including the heart, liver, spleen, lungs, and kidneys, using Hematoxylin and Eosin (H&E) staining (Figure 1j). No discernible alterations in physiological morphology were observed in mice treated with the nanoparticles, suggesting a favorable biosafety profile. Collectively, these findings confirm the excellent safety profile of the MiSp based nanoparticles, underscoring their potential for biomedical applications. The absence of cytotoxic, hemolytic, and organ-specific adverse effects indicates that these complex nanoparticles are promising candidates for further development in biomedicine as nanovaccines.

2.2. MiSp-Based Nanovaccines Significantly Enhance Antigen Uptake and Dendritic Cell (DC) Activation In Vitro

Considering the crucial role of efficient internalization in activating the immune system, we proceeded to evaluate the uptake of the different formulations by APCs. BMDCs were exposed to Cy5.5-labeled NM-VP1$^{T/B}$ nanoparticles, RA@NM-VP1$^{T/B}$ nanoparticles, or free VP1 protein, and the internalization of these formulations was observed and assessed by confocal microscopy. Interestingly, both nanovaccine groups (NM-VP1$^{T/B}$ and RA@NM-VP1$^{T/B}$ nanoparticles) significantly increased cellular uptake, exhibiting a seven-fold higher internalization compared to the free VP1 protein after a 1 h incubation period with BMDCs (**Figure** 2a,b), while the loading of RA on the nanoparticles did not lead to obvious effects on the uptake efficiency (Figure 2b).

Next, we explored whether the nanovaccines can enhance the antigen cross-presentation, a crucial mechanism for activating naïve CD8$^+$ T cells to target and eliminate pathogen-infected cells, and the escape of antigens from endo-lysosomal compartments significantly enhances cross-presentation. To assess whether the nanovaccines were localizing within cell lysosomes—sites of high enzymatic activity, including cathepsins S—a lysosomal marker (Lyso-Tracker) was utilized. Prominent yellow fluorescence, resulting from the merging of nanovaccine (red) and lysosomal (green) signals, was observed at 1 h exposure (Figure 2c; Figure S2, Supporting Information), indicating the co-localization of nanovaccines with lysosomes. After 5 h of exposure, the isolation of fluorescence signals between the antigen and lysosomes became apparent, suggesting antigen escape into the cytoplasm. This efficient uptake, subsequent localization within lysosomes, and escape into the cytoplasm might imply that the nanovaccines are adept at releasing peptides through cleavage at a specifically designed substrate site post-endosomal uptake by antigen-presenting cells, thereby facilitating antigen cross-presentation and subsequent T cell-mediated immune responses.

Moreover, the maturation and activation of BMDCs following exposure to various formulations were investigated by measuring the expression of costimulatory molecules (MHC class II, CD80, and CD86, Figure S3, Supporting Information). The expression of surface molecules linked to DC maturation (MHC class II) and activation (CD80 and CD86) were significantly elevated in cells treated with the nanovaccines (NM-VP1$^{T/B}$ or RA@NM-VP1$^{T/B}$ nanoparticles) (Figure 2d–f). Consequently, the MiSp based nanoparticle, utilized as a carrier for peptide vaccines, emerges as a potent adjuvant, enhancing the uptake, activation, and cross-presentation by APCs. However, the nanoparticles themselves (NM nanoparticles) did not elicit any upregulation of co-stimulatory factors, indicating that the MiSp nanoparticle does not trigger nonspecific immune activation. Additionally, we evaluated the expression level of CCR9 on BMDCs, given its importance in directing lymphocytes toward the gut. In comparison to treatments with VP1, RA@NM-VP1$^{T/B}$ nanovaccines significantly upregulated CCR9 expression, whereas NM-VP1$^{T/B}$ nanovaccines did not exhibit this effect (Figure 2g), underscoring the role of loaded RA on NM-VP1$^{T/B}$ nanoparticles in modulating CCR9 expression. Collectively, these results demonstrated that RA@NM-VP1$^{T/B}$ nanovaccines not only enhances antigen uptake and the maturation of DCs but also facilitates lysosomal escape for effective antigen cross-presentation and boosts the expression of gut-homing receptor CCR9 on DCs, highlighting the potential of the nanovaccines for initiating robust cellular and mucosal immune responses.

Figure 1. Characterization and biosafety evaluation of the chimeric nanoparticles. a) Observation of the different types of chimeric nanoparticles under SEM, the scale bar is 1 µm. b) The diameter (black), poly dispersity index (PDI, teal), and zeta potential (pink) of the nanoparticles were analyzed by DLS. c,d) The NM-VP1$^{T/B}$ nanoparticles loaded with different amount of RA were co-incubated with BMDCs for 24 h for optimizing the dose effects of RA in vitro. The cells were collected and analyzed by flow cytometry on the levels of CD86$^+$. IL-10 concentrations in the supernatant were analyzed by ELISA (d). e) Release behavior of RA from the loaded nanoparticles. The RA@NM-VP1$^{T/B}$ nanoparticles were incubated under pH 5.0 (endosomes) and pH 7.4 (cytosolic delivery), respectively, for 60 h, and the released RA was measured. f,g) Cell viability was assessed at different time points (24, 48, and 72 h, also applies to panel g) on RAW264.7 (f) and BMDC (g) cells using the CCK-8 Cell Proliferation Assay Kit ($n = 3$) for the different chimeric nanoparticles. h) Cytokine measurement in the serum of mice immunized with PBS, RA@NM-VP$^{T/B}$ or lipopolysaccharide (LPS) using ELISA assay ($n = 3$). i) Hemolytic activities of the nanoparticles at different concentrations. Mice RBCs were incubated with the nanoparticles for 30 min at 37 °C and the mixture was centrifuged to detect the cell-free hemoglobin in the supernatant. % Hemolysis was calculated using Triton X-100 as the positive control ($n = 3$). j) Histological section of mice heart, liver, spleen, lung and kidney after three times repeated intravenous administrations of nanovaccines (300 µg per mice), while the PBS was used as control. The sections were stained with hematoxylin eosin and the scale bar is 100 µm. The data are presented as mean ± SD. Statistical analysis via one-way analysis of variance (ANOVA): $^{**}p < 0.01$; $^{***}p < 0.001$, ns, not significant.

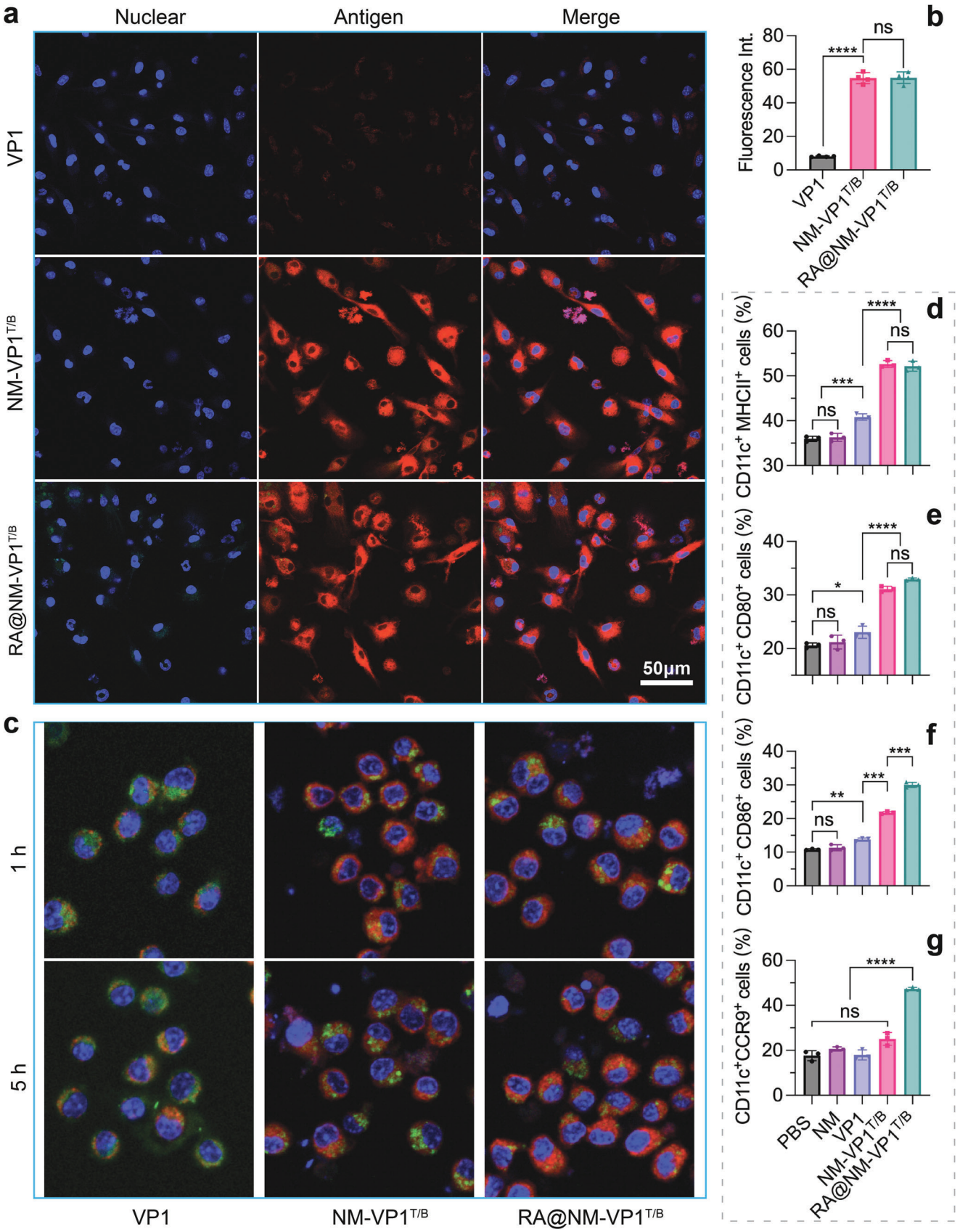

2.3. In Vivo Delivery and Immune Activation at the Injection Site

To investigate the in vivo delivery and immune activation at the injection site, the persistence of the antigen at the injection sites was monitored at various time intervals using an animal in vivo imaging system. For tracking and visualizing the different formulations, antigens were labelled with the fluorescent dye Cy5.5 and injected subcutaneously into mice. At 48 h post-injection, only a faint fluorescence from VP1 group was detectable, whereas both NM-VP1$^{T/B}$ and RA@NM-VP1$^{T/B}$ nanovaccine groups exhibited strong and sustained signals in the abdomen up to the 96 h point (**Figure** 3a,b). These observations suggest that the formulated nanovaccines are able to create a robust antigenic reservoir effect at the injection site, potentially enhancing immune cell recruitment. Given the notable differences in antigen persistence profiles at the injection sites, we further explored the transport of antigens into draining lymph nodes (LNs) among the various formulations. Mice were received subcutaneous injections of the specified Cy5.5-labeled formulations, and the draining LNs were harvested for ex vivo fluorescence analysis 24 h post-immunization. The VP1 group showed minimal Cy5.5 signals, whereas the nanovaccine groups (NM-VP1$^{T/B}$ or RA@NM-VP1$^{T/B}$ nanoparticles) demonstrated significantly higher fluorescence accumulation in the draining LNs (Figure 3c–e), indicating an efficient nanovaccine transport to LNs. These results imply that these nanovaccines are able to maintain the retention at the injection site and facilitate continuous antigen delivery to the draining LNs. Consequently, the recruitment, activation, and gut-tropism effects on peripheral DCs in the draining LNs were assessed. Subsequent analysis of MHC molecules (MHC II) and costimulatory molecules (CD80 and CD86) expression on DCs in draining LNs via flow cytometry revealed that the populations of CD11c$^+$MHCII$^+$, CD11c$^+$CD80$^+$, and CD11c$^+$CD86$^+$ significantly increased compared to the free antigen groups (nanovaccine group vs VP1 group), with no marked differences observed between the two nanovaccine formulations (Figure 3f–h; Figure S4, Supporting Information). Leveraging the upregulation of gut homing receptors (CCR9), which enables DCs to migrate toward the intestinal mucosa following the CCL25 concentration gradient, we assessed LN-tropism by quantifying CD11c+ cells expressing CCR9. The RA@NM-VP1$^{T/B}$ formulation induced a significant increase, ≈1.7-fold, in CD11c$^+$CCR9$^+$ DCs compared to both VP1 and NM-VP1$^{T/B}$ (Figure 3i), showcasing its capability for gut homing. The subset of CD103$^+$CD11b$^+$ DCs, crucial for SIgA production and considered the primary migratory DC population, were markedly recruited into mesenteric lymph nodes (MLNs) 48 h post-immunization by RA@NM-VP1$^{T/B}$. Notably, the presence of CD103$^+$CD11b$^+$ DCs in the MLNs of the RA@NM-VP1$^{T/B}$ group shown a 1.85-fold increase over the NM-VP1$^{T/B}$ group (Figure 3j), indicating that the RA-loaded nanovaccine not only activated DCs but also facilitated their migration to the MLN along the CCL25 gradient. These results collectively reveal that RA@NM-VP1$^{T/B}$ efficiently targets lymph nodes, boosts DC uptake, and significantly increases CCR9 expression on DCs, facilitating the subcutaneous-to-intestinal immune cascade. This positions RA@NM-VP1$^{T/B}$ as a promising vehicle for enhancing humoral immunity and initiating mucosal immune responses.

2.4. Systemic and Mucosal Immune Responses in Mice

To assess the immune effects, the efficacy of the adaptive immune response elicited by the nanovaccines was assessed in vivo. Balb/c mice were administered subcutaneous vaccinations with the specified formulations containing 25 μg antigen on days 0, 14, and 28 (**Figure** 4a). Seven days following the final vaccination, sera were collected. The CVB3 VP1 protein, purified from *E. coli*, was served as the antigen to quantify VP1-specific antibodies. Interestingly, mice vaccinated with the nanovaccine formulations (NM-VP1$^{T/B}$ or RA@NM-VP1$^{T/B}$ nanoparticles) exhibited significantly elevated titers of VP1-specific serum immunoglobulin G (IgG) compared to all other groups, with NM-VP1$^{T/B}$ and RA@NM-VP1$^{T/B}$ showing equivalent antibody levels (Figure 4b). Conversely, minimal VP1-specific antibody responses were observed in mice immunized with either the VP1 protein alone or a simple mixture of VP1 and RA (RA@VP1) (Figure 4b).

An optimal vaccine not only provokes antibody production but also stimulates CD4$^+$ T cells to differentiate into helper T cell subsets, such as Th1 and Th2 cells, crucial for activating cytotoxic T lymphocytes (CTLs) or B cells. To examine the immune polarization, we measured the levels of antigen-specific IgG1 and IgG2a subclasses in three animal groups using ELISA (VP1, NM-VP1$^{T/B}$ or RA@NM-VP1$^{T/B}$ nanoparticles). IgG1 predominantly contributes to virus neutralization, whereas IgG2a production indicates a Th1-polarized immune response. The ratio of IgG2a/IgG1 serves as a marker for a Th1-biased immune response. Both nanovaccine formulations induced significantly higher IgG1 and IgG2a levels compared to the soluble antigen (VP1) (Figure 4c,d), with NM-VP1$^{T/B}$ and RA@NM-VP1$^{T/B}$ producing comparable IgG2a/IgG1 ratios (Figure 4e), indicative of a mixed Th1 and Th2 immune response.

Furthermore, the neutralizing capability of sera containing antigen-specific antibodies against CVB3 was investigated with the Viral Neutralization assay. Sera from the nanovaccine-treated groups demonstrated superior neutralization activity against CVB3 infection compared to the VP1-treated groups (Figure 4f). Additionally, the binding strength (avidity) between the antigen and IgG antibodies in the serum was assessed by ELISA combined with a urea-elution step. Notably, the avidity index of serum IgG elicited by the nanovaccine was significantly higher than that of the VP1 group (Figure 4g), indicating that the nanovaccine formulations generated a more potent and higher quality antigen-specific IgG antibody response than the VP1 protein alone. Considering the critical importance of secretory IgA (SIgA) in mucosal protection, we evaluated the ability of RA-loaded nanovaccines to stimulate a mucosal immune response. Strikingly, the

Figure 2. Antigen uptake and the maturation of BMDCs. BMDCs were cultured with Cy5.5-labeled VP1 protein or Cy5.5-labeled nanoparticles (NM-VP1$^{T/B}$ or RA@NM-VP1$^{T/B}$) for 2 h. a) Representative confocal images of BMDCs internalization of different vaccine formulations, and the fluorescence intensities were quantified with Image J ($n = 4$). The scale bar is 50 μm. c) Confocal laser scanning images of internalization and trafficking of BMDCs co-cultured with different Cy5.5 (red) labeled formulations for 1 or 5 h (also see Figure S2, Supporting Information). Nuclei were stained with DAPI (blue), lysosomes were stained with LysoTracker Green (Green). d–g) The percentage of MHCII, CD80, CD86, and CCR9 from BMDCs after incubating with the different formulations for 24 h ($n = 4$). Data are presented as mean ± SD. *$p < 0.05$, **$p < 0.01$, ***$p < 0.001$, and ****$p < 0.0001$.

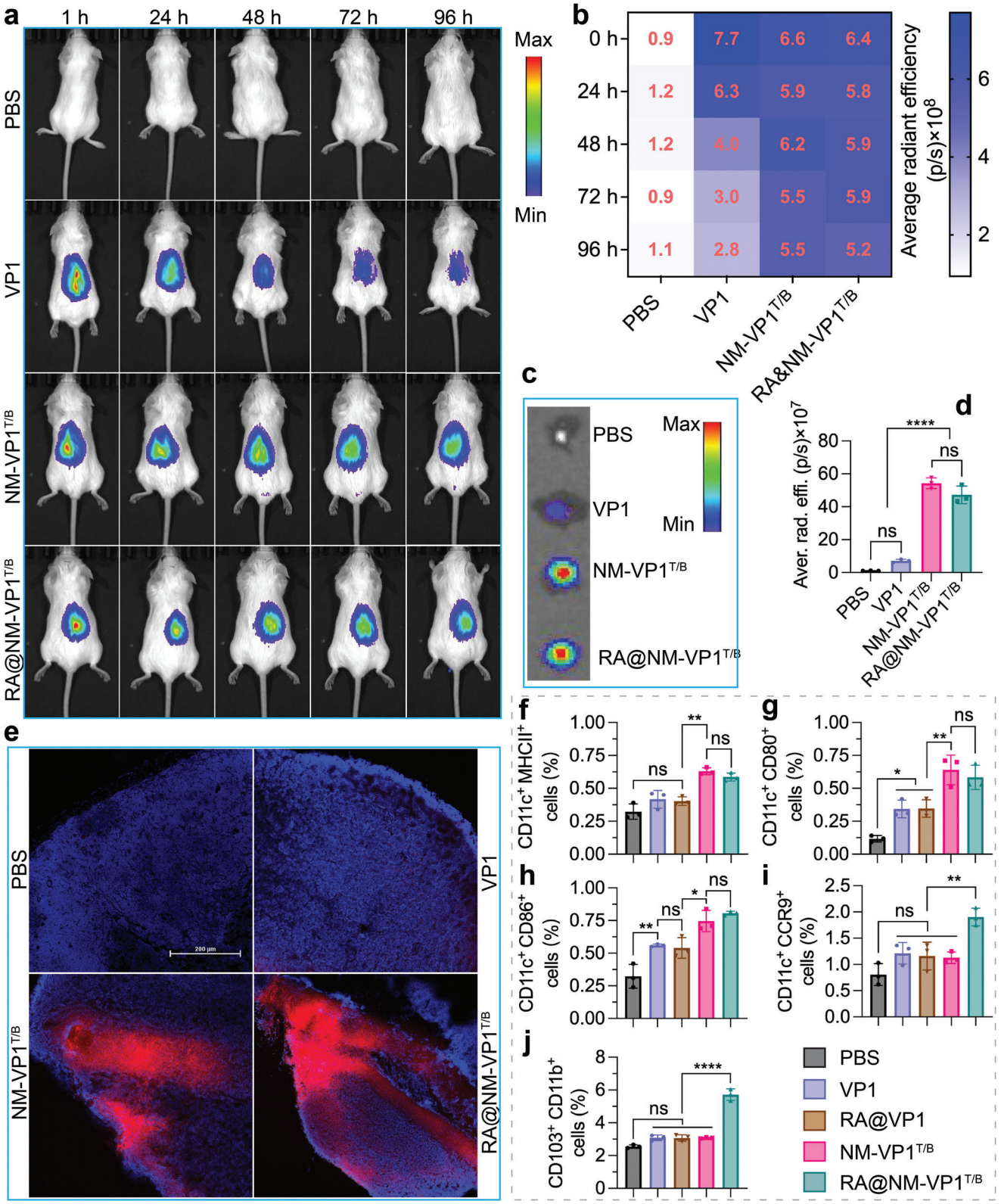

Figure 3. Nanovaccines delivery into draining lymph nodes and effects on dendritic cell maturation. a) In vivo imaging of nanovaccines at different time intervals following subcutaneously injection at the dorsal flanks. b) Heatmap of the fluorescent intensities of different formulations persisting at the injection site. c) Ex vivo fluorescence imaging of nanovaccines migration to draining lymph nodes after subcutaneously injection for 24 h. d) Quantitation of fluorescence intensities in draining lymph nodes. e) Fluorescence imaging of the labeled antigen in the slice of draining lymph nodes. The scale bar is 200 μm. f–h) Effects of nanovaccines on dendritic cell maturation in draining lymph nodes after subcutaneously injection for 36 h. The percentages

RA@NM-VP1$^{T/B}$ group produced significantly higher levels of SIgA compared to all other formulations (Figure 4h). In contrast, a mere mixture of RA with the free antigen (RA@VP1) did not enhance SIgA production. While the nanovaccine formulations induced a comparable systemic immune response, RA@NM-VP1$^{T/B}$ efficiently stimulated SIgA production (Figure 4h). These findings suggest that RA in solution was insufficient for APC targeting and that co-delivery of antigens and RA within a single carrier is crucial for enhancing the expression of gut-homing receptors CCR9 on DCs, thereby facilitating the migration of activated lymphocytes to the intestine and eliciting potent mucosal immune responses.

2.5. Nanovaccine Induces Cell-Mediated Immune Response

Mice were subcutaneously immunized with various vaccine formulations (PBS, VP1, NM-VP1$^{T/B}$ or RA@NM-VP1$^{T/B}$ nanoparticles) at two-week intervals for a total of three doses, with spleens collected seven days post-final immunization (Figure 4a). Splenocytes were subsequently restimulated ex vivo with the VP1 protein for 72 h. Given the pivotal role of cytokines in combating CVB3 infection, we quantified the expression of IFN-γ, TNF-α, IL-4, and IL-6 in the culture supernatants of splenocytes using the ELISA assay. IFN-γ and TNF-α, primarily secreted by Th1 cells, play a vital role in eliminating infected cells, whereas IL-4 and IL-6 are key to Th2-mediated humoral immune responses.[44,45] The results revealed that cytokine levels in the nanovaccine groups were significantly higher than those in the VP1 or the PBS group (Figure 4i), indicating an enhanced cell-mediated immune response. These results are not necessarily contradictory to the observation—no significant difference in the levels of VP1-specific IgG1 and IgG2a between the RA@NM-VP1$^{T/B}$ and NM-VP1$^{T/B}$ groups (Figure 4d,e,i), as the production of IgG1 and IgG2a antibodies can be influenced by various factors, including the presence of specific cytokines, but it does not solely depend on the levels of IL-4 and IL-6. Notably, the RA@NM-VP1$^{T/B}$ and NM-VP1$^{T/B}$ nanoparticle treatments produced similar levels of IFN-γ and TNF-α, but elevated levels of IL-4 and IL-6 were observed for the RA loaded nanovaccines, suggesting that the nanovaccine formulations, in particular the RA loaded ones, are capable of eliciting a potent mixed Th1 and Th2 immune response. Furthermore, CVB3-specific T-cell proliferation and the magnitude of CTL responses post-vaccination were assessed via the EdU incorporation assay and the lactate dehydrogenase (LDH) release assay, respectively. Aligning with the intracellular cytokine assay outcomes, both CTL responses (Figure 4j) and CVB3-specific T-cell proliferation (Figure 4k,l) were significantly higher in the nanovaccine groups compared to the VP1 group. The effects between RA@NM-VP1$^{T/B}$ and NM-VP1$^{T/B}$ were comparable, reinforcing the notion that nanovaccine immunization effectively promotes VP1-specific T-cell activation and proliferation, and significantly boosts systemic CTL responses. These observations underscore the efficacy of nanovaccine formulations in inducing a comprehensive immune defense against CVB3.

2.6. Protection Efficacy Against CVB3 Challenge

Encouraged by these promising outcomes, we next assessed the protective efficacy of the RA@NM-VP1$^{T/B}$ nanovaccine against CVB3 infection in mouse models. Mice were exposed to a 3LD50 dose of CVB3 one week following the third immunization (**Figure 5a**), with myocarditis severity gauged through metrics such as body weight loss, viral titers in the heart, and cardiac histopathology. Remarkably, the group immunized with the nanovaccine exhibited minimal body weight loss (Figure 5b) and minimal cardiac viral load (Figure 5c), distinguishing it from the other groups. This heightened immunoprotection is attributed to the nanovaccine's superior viral containment within the heart, as evidenced by improved cardiac functions, notably in increased Left Ventricular Ejection Fraction (LVEF) and Left Ventricular Fractional Shortening (LVFS) (Figure 5d–f). Correspondingly, the nanovaccine-immunized mice displayed the least cardiac inflammatory infiltration and necrosis, with myocardial inflammation present ≈20% of the tissue examined for the RA loaded nanovaccines. In contrast, mice immunized with the VP1 protein alone developed significantly more severe myocarditis, with inflammation levels nearing 50% but no significant difference from the control group (Figure 5g,h).

Both nanovaccine formulations, RA@NM-VP1$^{T/B}$ and NM-VP1$^{T/B}$ nanoparticles, conferred the enhanced degree of protection against CVB3 infection, in particular the RA-load ones. To further assessed the protective effects, the mice were exposed to a lethal dose of CVB3 following the last immunization (Figure 5a). Interestingly, following the lethal dose of CVB3, the RA@NM-VP1$^{T/B}$ nanovaccines showed the highest survival rate up to 50%, surpassing NM-VP1$^{T/B}$ (37.5%) and significantly outperforming the VP1 group, where only 12.5% of mice survived. All mice in the PBS group succumbed within 10 days (Figure 5i). These results underscore the capability of MiSp based nanovaccines to provide efficient immunoprotection against CVB3 challenge by eliciting an effective mucosal response, which is further enhanced by RA loading, showcasing its potential as a formidable candidate in the fight against CVB3 infection.

3. Discussion

In light of the significant reduction in the incidence of severe diseases associated with CVB3 infection that vaccination can achieve, and despite the development of various types of CVB3 vaccines in recent years, there currently remains a lack of clinically approved vaccines or therapeutic agents. A common objective among these vaccine developments is the potent induction of both humoral and mucosal immune responses. In this study, we developed spidroin-based nanovaccines aimed at preventing CVB3-induced viral myocarditis. The formulation (NM-VP1$^{T/B}$) successfully induced substantial VP1-specific IgG secretion, simultaneously promoted Th1 and Th2 immune responses, and enhanced cell-mediated immunity. To foster mucosal immune responses through conventional subunit vaccines, we explored delivery of the antigen with RA-loaded nanovaccine to

of MHCII$^+$, CD80$^+$, and CD86$^+$ positive cells in CD11C$^+$ DCs of lymph nodes cells were evaluated by flow cytometry. i) The percentages of CCR9 in CD11c+ DCs of draining lymph nodes cells measured by flow cytometry. j) The percentages of CD103$^+$CD11b$^+$ DCs collected from MLNs 36 h post subcutaneously immunization. Data are presented as mean ± SD ($n = 3$). *$p < 0.05$, **$p < 0.01$, and ****$p < 0.0001$.

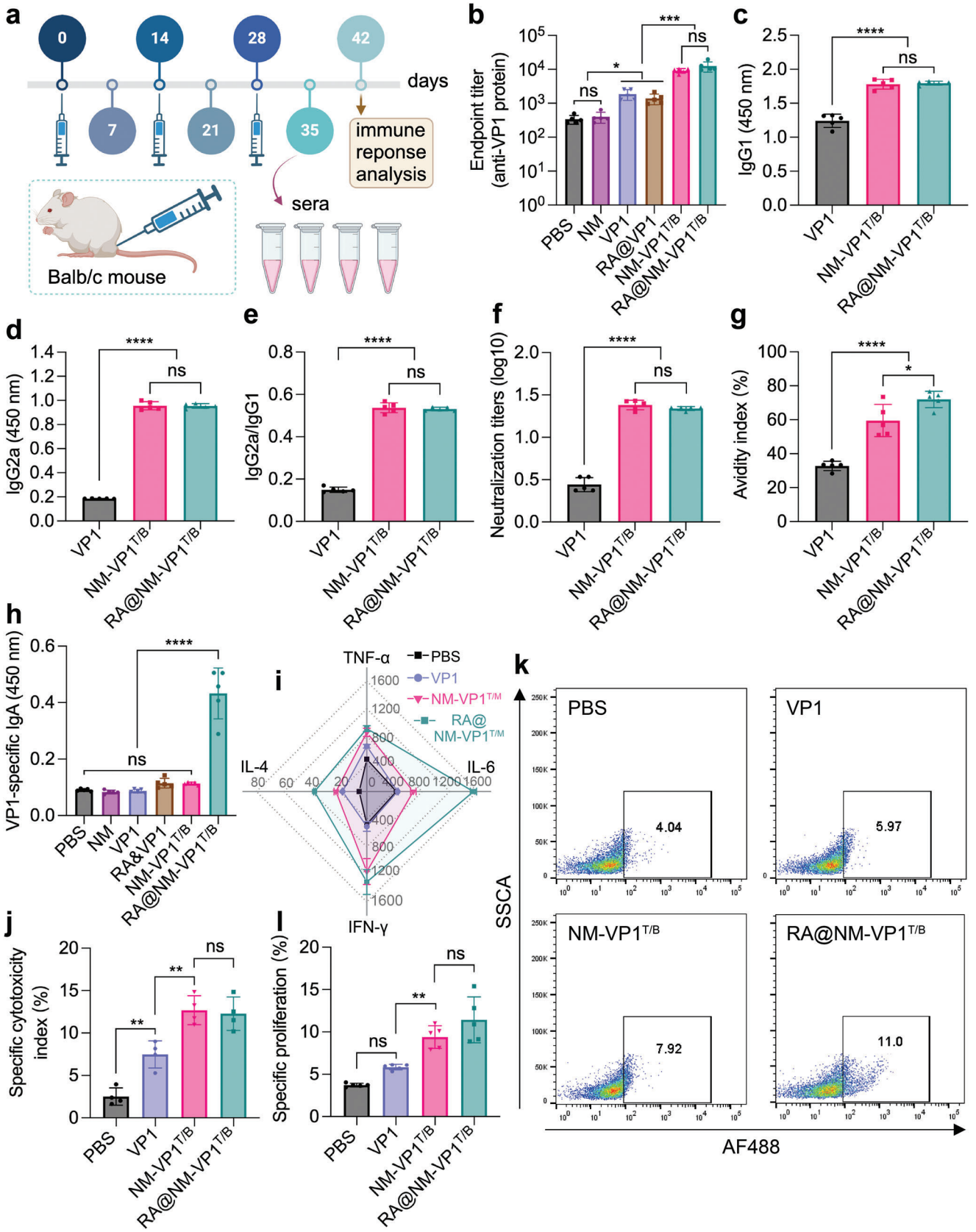

bypass tissue-specific barriers. The RA@NM-VP1$^{T/B}$ notably induced significant VP1-specific IgA secretion in the intestinal mucosa, alongside elevated titers of antigen-specific IgG secretion and cellular immune responses, showcasing its immunogenic efficacy (Figure 4). This approach is unique in directly connecting RA with spider silk-based nanoparticles for the co-delivery of peptide antigens, which only requires a low dose of RA to induce both humoral and mucosal immune responses, different from previous studies showing that high dose of RA (>300 μg) is necessary for the separate delivery of antigen and RA to lymph nodes to induce SIgA generation.[8,10]

Nanoparticles derived from spidroin stand out for their biocompatibility and biodegradability, facilitating controlled release of encapsulated agents for a sustained effect.[34,46–49] Nonetheless, the encapsulation efficiency of such nanoparticles is influenced by electrostatic interactions and molecular parameters. The CVB3 capsid protein VP1, characterized by an isoelectric point of 9.0 and a molecular weight of 32 kDa, showed less than 10% loading efficiency onto NM NPs. To overcome these challenges, we engineered hybrid proteins by fusing a B-cell and a T-cell epitope peptides from the CVB3 VP1 protein to the C-terminus of recombinant spider silk protein NM, linked by a cathepsin S-cleavable linker. This approach has demonstrated high biocompatibility and facilitated the formation of hybrid nanoparticles (NM-VP1$^{T/B}$) through salting out, showing promise for enhanced immune responses. Antigen-presenting cells, such as macrophages and dendritic cells, are known for their high enzymatic activity of cathepsins B and S within the endosome, playing a pivotal role in antigen processing.[44,45] The effective uptake and lysosomal targeting of the nanoparticles in BMDCs suggest that the engineered chimeric proteins might be primed for cleavage at the specifically designed substrate site (cathepsin S substrate linker, PMGLP) following endosomal uptake. Furthermore, the facilitated escape of antigens from the endo-lysosomal compartment into the cytoplasm significantly enhances cross-presentation, a vital mechanism for triggering cellular immune responses. Although the underlying mechanism is unclear, the RA@NM-VP1T/B nanovaccine facilitates lysosomal escape might be through several potential mechanisms, including 1) the unique composition and structure of the MiSp based nanoparticles might promote efficient endocytosis and interaction with lysosomal membranes, potentially destabilizing them; 2) the cathepsin S substrate linker allows proteolytic cleavage, disrupting lysosomal integrity; 3) RA modulates immune responses, enhancing dendritic cell maturation and altering endosomal-lysosomal dynamics to favor antigen escape; 4) the sustained release of RA and antigens further supports continuous interactions with lysosomal membranes, increasing the likelihood of antigen escape into the cytoplasm. Activation and proliferation are essential for effective T-cell-mediated immune responses. In this context, this study notes a significant enhancement within the nanovaccine groups compared to the VP1 group. This improvement probably arises from exosome-like particles being internalized and presented by dendritic cells more efficiently, which enhances CTL activation, coupled with the gradual and constant antigen release from the exosomes, crucial for a robust and sustained induction of CTL responses.[50–52] These results position the RA@NM-VP1$^{T/B}$ formulation as a potent platform for initiating both cellular and mucosal immune responses, effectively enhancing the efficacy of parenteral vaccinations against pandemic gastrointestinal infections by bolstering humoral and mucosal immune responses.

Immunization with NM-VP1$^{T/B}$ and RA@NM-VP1$^{T/B}$ not only elicited a more robust protective serum IgG antibody response but also enhanced the induction of specific cytotoxic CTLs. Moreover, the RA@NM-VP1$^{T/B}$ formulation demonstrated a mucosal immune response, leading to superior control of CVB3 infection and a more effective prophylactic impact against viral myocarditis. The nanovaccines presented in this research offer several benefits: first, NM-VP1$^{T/B}$ and RA@NM-VP1$^{T/B}$ are capable of targeting lymph nodes, improving DC uptake, and fostering DC activation and maturation to bolster the humoral immune response. Despite the size of RA@NM-VP1$^{T/B}$ nanoparticles, the targeting of lymph nodes might be attributed to a combination of the enhanced permeability and retention effect, active cellular transport mechanisms, surface properties of the nanoparticles, and natural lymphatic flow dynamics. Second, they amplify antigen cross-presentation, enhancing virus-specific CD8$^+$ T-cell responses for the clearance of virus-infected cells. Third, RA@NM-VP1$^{T/B}$ efficiently upregulates CCR9 expression on DCs, facilitating the subcutis-to-intestine cascade and initiating mucosal immune responses. These results suggest that RA@NM-VP1$^{T/B}$ could be a promising vaccine candidate against CVB3-induced viral myocarditis. However, our research also identifies certain limitations and areas for further investigation, including a need for deeper insight into the specific molecular and immunological mechanisms through which RA@NM-VP1$^{T/B}$ enhances antigen cross-presentation. Additionally, it is yet to be determined whether periodic booster vaccinations are necessary to maintain the vaccine's protective efficacy. Addressing these questions is crucial for the continued advancement and development of novel anti-CVB3 vaccines based on the RA@NM-VP1$^{T/B}$ platform.

4. Experimental Section

Mouse Model, CVB3 Virus, and Cell Culture: All experimental protocols and animal analyses were conducted in accordance with the Guide

Figure 4. RA@NM-VP1$^{T/B}$ nanovaccines stimulate humoral and mucosal immune responses. a) Male Balb/c mice were immunized subcutaneously with different vaccine formulations at the base of their tails with 100 μL of various vaccine formulations, each containing 25 μg of antigen. Mice were immunized 3 times at 2-week intervals (day 0, 14, and 28), serum samples collected at 7 days after the last immunization (day 35), and spleen for each mouse was collected at day 42. b) Serum VP1-specific IgG antibody titers. c,d) The levels of VP1-specific IgG1 and IgG2a subclasses, diluted for 1:40 and measured at 450 nm. e) The ratio of serum VP1-specific IgG2a and IgG1 levels. f) Levels of serum neutralizing antibody in immunized mice. g) VP1-specific IgG antibody avidity. h) Anti-VP1 SIgA level in intestinal wash. i) Splenocytes from the vaccination mice were stimulated with VP1 protein for 72 h and the supernatants were collected. The expression of IFN-γ, TNF-α, IL-4, and IL-6 cytokines were analyzed using ELISA assay. j) CVB3-specific cytotoxicity responses of splenic cells were detected by the LDH assay using VP1-transfected autologous SP2/0 cells as target cells. l) The isolated splenocytes from immunized mice were stimulated with 10 μg mL^{-1} VP1 protein for 72 h and detected by an EdU-488 Cell Proliferation Assay Kit. k) The representative flow cytometry for splenocytes specific proliferation. Data are presented as mean ± SD ($n = 5$). *$p < 0.05$, **$p < 0.01$, and ****$p < 0.0001$.

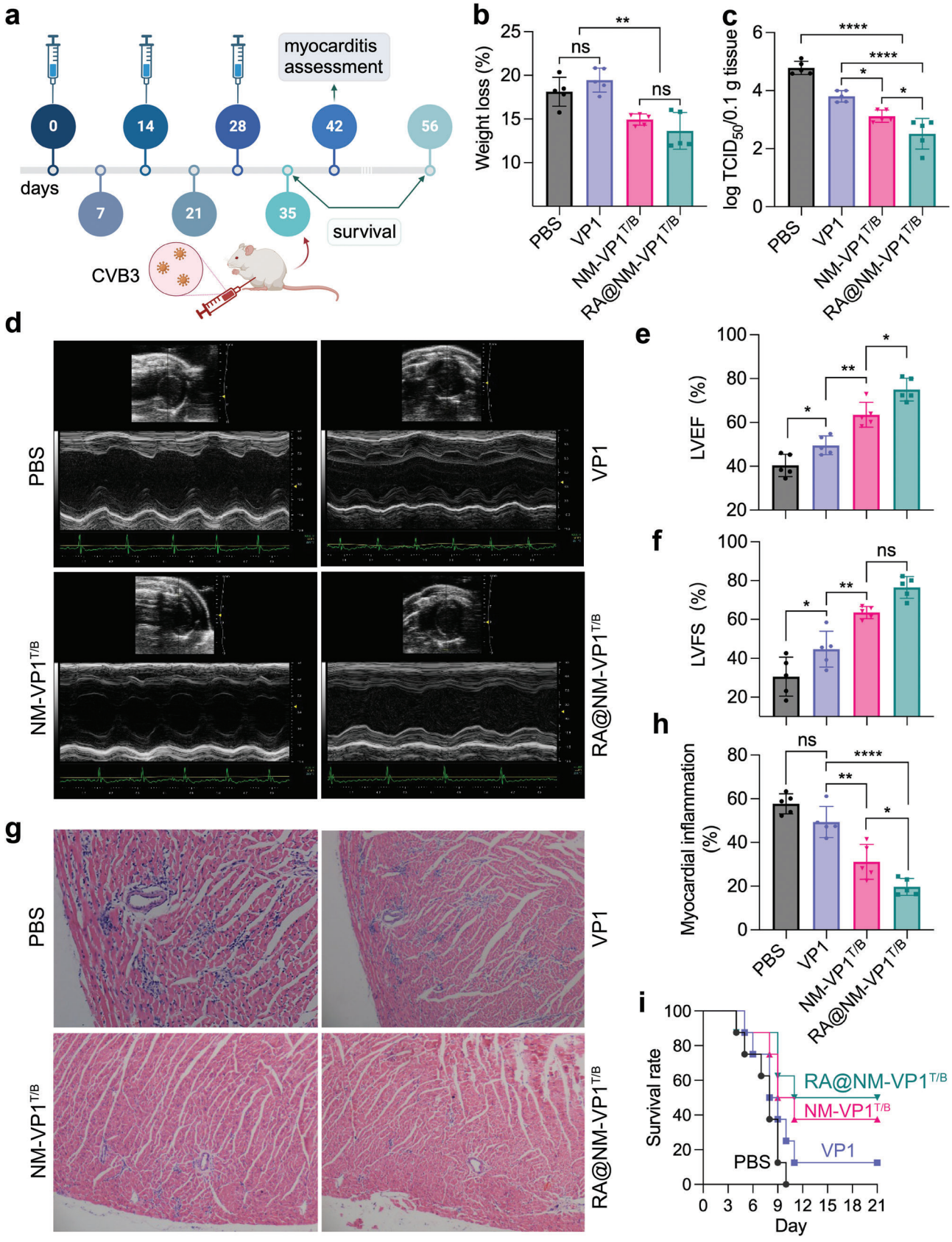

for the Care and Use of Medical Laboratory Animals (Ministry of Health, China), and received ethical approval from Soochow University. BALB/c mice, aged 6–8 weeks, were purchased from the Experimental Animal Center of the Chinese Academy of Science (Shanghai, China). The CVB3 virus (Nancy strain) used in the experiments was maintained and propagated in the laboratory through passages in HeLa cells.

Human embryonic kidney 293T cells (HEK293T), HeLa cells, and RAW264.7 cells were cultured in Dulbecco's Modified Eagle's Medium (DMEM, Hyclone), while Sp2/0 cells (mouse myeloma cells) were cultured in RPMI-1640 medium (Hyclone). Both media were supplemented with 10% fetal bovine serum (FBS, Gibco), 2 mM L-glutamine, and 1% penicillin/streptomycin (Invitrogen). Culturing occurred in a controlled environment with 5% CO_2 at 37 °C in an incubation chamber. BMDCs were generated as previously described.[53] Briefly, femurs and tibias were sterilized with 70% ethanol and red blood cell (RBC)-depleted bone marrow cells from Balb/c mice were seeded into 24-well plates at a density of 1×10^6 cells per well in complete RPMI media. This medium was supplemented with 20 ng mL^{-1} murine recombinant granulocyte-macrophage colony-stimulating factor (GM-CSF). On days 3 and 6, half of the culture supernatant was replaced with fresh RPMI 1640 medium containing the same concentration of GM-CSF. By day 8, loosely and non-adherent cells were collected and used as inactivated BMDCs.

Protein Preparation: The chimeric protein sequences encoding NM-VP1^T and NM-VP1^B, respectively, were synthesized and cloned into the pET-32a plasmid using *Nde*I and *Xho*I restriction sites. These plasmids were subsequently transformed into *E. coli* BL21 (DE3) competent cells, which were cultured at 37 °C in LB medium supplemented with 100 μg mL. ampicillin. Growth continued until OD_{600} reached ≈0.8, after which the temperature was lowered to 25 °C and 1 mM Isopropyl *β*-D-Thiogalactoside (IPTG) was added to induce protein expression. The cells were incubated for an additional 12 h. For protein purification, the cells were harvested via centrifugation and lysed using a high-pressure homogenizer (PhD Technology LLC, USA). The resulting insoluble pellets were thoroughly washed three times with 30 mL of washing buffer (20 mM Tris, 300 mM NaCl, 1 mM EDTA, 1% Triton X-100, 1 M urea, pH 8.0). To remove any residual detergent, the purified inclusion bodies were finally rinsed with 20 mM Tris (pH 8.0) and solubilized using a freeze-thaw method.[54] Specifically, the pellet was resuspended in 2 M urea, frozen at −20 °C, and thawed at room temperature. Following centrifugation at 12,000 g for 20 min, the supernatant was collected and subjected to SDS-PAGE analysis (Figure S1c, Supporting Information). Protein concentration was determined using Pierce BCA Protein Assay Kits (Thermo Scientific, USA).

Nanoparticle Preparation and Characterization: The lyophilized proteins NM-VP1^B and NM-VP1^T were dissolved in 6 M guanidinium chloride and then dialyzed against 10 mM Tris/HCl. Subsequently, the samples were centrifuged to remove any remaining aggregates and passed through a 0.2 μm filter for filtration. For in vitro and in vivo studies, endotoxins were removed from the proteins using an Endotoxin Removal Kit (Yeasen, China), and protein concentrations were determined using a BCA Protein Assay Kit (Thermo Scientific, USA). Nanoparticles (NM-VP1^B and NM-VP1^T) were prepared by the salting-out method using a potassium phosphate solution (Figure S1d, Supporting Information), as previously described.[41–43] Briefly, the protein solution (2.5 mg mL^{-1}) was mixed with potassium phosphate (2 M, pH 8.0) in a volumetric ratio of 1:10 using a pipette for 2 h at room temperature. The resulting nanoparticles were then washed three times with MilliQ water, and the nanoparticle concentrations were determined gravimetrically. The nanoparticle suspension was sonicated for 5 min and diluted just before measurement to a concentration of 0.01 mg mL^{-1}. Particle size, PDI, and zeta-potential were analyzed using a Nano Zetasizer (Malvern Instruments, Worcestershire, UK). The morphology of the nanoparticles was examined using SEM (S-4700, Hitachi, Japan). Fluorescently labeled nanoparticles for in vivo and in vitro studies were prepared by adding a ten-fold molar excess of Cy5.5 NHS ester (Aladdin, China) to the nanoparticle suspension. This mixture was incubated for 12 h in the dark. Following incubation, the nanoparticles were centrifuged and washed three times with MilliQ water. Finally, the nanoparticles were resuspended in 10 mM PBS at pH 7.4 to achieve a concentration of 1 mg mL^{-1}.

RA Loading and Releasing: A stock solution of all-trans retinoic acid (RA) was prepared by dissolving 10 mg of RA (Solarbio, China) in 1 mL of DMSO, resulting in a concentration of 10 mg mL^{-1}. To prepare RA-loaded nanoparticles, 1 mg of either NM-VP1^B or NM-VP1^T nanoparticles were mixed with varying concentrations of the RA solution (40–80 μg mL^{-1}) and incubated at 4 °C for 2 h. Subsequently, the mixture was centrifuged at 12,000 rpm for 20 min and washed three times with PBS to remove unbound RA and quantified at the absorbance of 297 nm using a microplate reader (Thermo Scientific, USA). The loading rate of RA was calculated using a standard formula.

$$\text{loading}\left(\frac{\text{w}}{\text{w}}\%\right) = \frac{\text{weight of RA in nanoparticles}}{\text{weight of nanoparticles}} \times 100\% \quad (1)$$

The in vitro release of RA from nanoparticles was investigated at pH levels of 5.0 and 7.4, respectively. The RA-loaded nanoparticles (RA@NM-VP1$^{T/B}$, 1 mg mL^{-1}) was dispersed in PBS and maintained at 37 °C with stirring at 130 rpm. At specified time intervals, the samples were centrifuged at 12,000 rpm for 20 min. The supernatant was then analyzed for the total released RA by measuring the absorbance at 297 nm. After each measurement, the supernatant was replaced with fresh release buffer. This procedure was repeated in triplicate across a duration of 60 h.

Nanovaccine Biosafety Assay: The cytotoxicity of nanovaccines in RAW264.7 and BMDC cells was evaluated using the CCK-8 Cell Proliferation Assay Kit (NCM Biotech, China). Cells were seeded at a density of 1×10^5 cells per well in 96-well plates. Subsequently, 10 μL of nanovaccine were added in triplicate to achieve final concentrations of 100, 200, 500, and 1000 μg mL^{-1}, with PBS serving as a control. After 24, 48, or 72 h of incubation, 10 μL of CCK-8 solution was added to each well and the plates were incubated for an additional 4 h at 37 °C. Cell viability was determined by measuring the absorbance at 450 nm using a microplate reader (Thermo Scientific, USA). Cell viability was calculated using the formula: cell viability (%) = (OD sample/OD control) × 100%. Untreated cells served as 100% cell viability. The levels of IL-1*β*, TNF-*α*, and IFN-*γ* in the serum of mice immunized with RA@NM-VP1$^{T/B}$ were quantified using ELISA. To evaluate hemolysis, whole blood was collected from mice and centrifuged to isolate red blood cells (RBCs). Nanovaccine samples were then incubated with a 4% RBC suspension at various concentrations. After 30 min incubation at 37 °C, the mixture was centrifuged at 800× g for 15 min, and the supernatants were collected for optical density measurements at 540 nm using a microplate reader. Triton X-100 treated RBCs served as the positive control. Hemolysis rate was calculated as: (OD sample group – OD negative control)/(OD positive control – OD negative control). In terms of tolerance, mice were divided into groups of three and received intravenous injections of 300 μg of nanovaccines suspended in 100 μL of PBS for three consecutive days. A control group was similarly injected with 100 μL of PBS. After 24 h from the last treatment, the mice were euthanized by decapitation. Heart, kidney, liver, lung, spleen, and small intestines were collected, fixed in 10% phosphate-buffered formalin, embedded in paraffin, sectioned, and stained with H&E for histological evaluation.

Figure 5. Immunoprotection against CVB3-induced viral myocarditis by immunization of the chimeric nanovaccines. a) Mice were challenged with 3LD50 CVB3 7 days after the final immunization at day 28, and myocarditis severity was evaluated 7 days later. For survival rate, the mice were injected with 5LD50 CVB3 after the final immunization and observed for 21 days. b) Body weight changes for the immunized mice. c) Viral load in the heart tissue of different mice. d–f) Cardiac function for each group was assessed by echocardiography using a cardiac function through a high-resolution ultrasound imaging system. g,h) Histomorphological changes of heart tissues and statistical analysis for the immunized mice followed by CVB3 infections. i) A 21-day survival rate was recorded after the 5LD50 CVB3 infection. For histomorphological observations, each group contained 5 mice. For survival rate evaluation, each group contained 8 mice. Data are presented as mean ± SD ($n = 5$). *$p < 0.05$, **$p < 0.01$, and ****$p < 0.0001$.

Cellular Uptake, BMDCs Activation, and Lysosomal Escape: BMDCs were seeded into 24-well plates at a density of 1×10^6 cells per well and incubated with a medium containing 10 μg mL^{-1} of either Cy5.5 labeled nanovaccine (NM-VP1$^{T/B}$, RA@NM-VP1$^{T/B}$) or Cy5.5 labeled VP1 protein. To observe cellular uptake, the cells were incubated for 1 h at 37 °C in a 5% CO2 incubator, then centrifuged, and the cell pellet was washed three times with PBS. The washed cells were subsequently examined using a confocal fluorescence microscope (Nikon, Japan). To evaluate the lysosomal escape ability, BMDCs were incubated for 1 and 5 h at 37 °C, respectively. The cells were subsequently stained with LysoTracker Green (Life Technologies, USA) and DAPI (Beyotime, China) to highlight the lysosomes and nuclei, respectively, and visualized using a confocal laser scanning microscope (Nikon, Japan). For assessing BMDC activation and CCR9 expression, the cells were exposed to different formulations for 36 h and then collected for flow cytometry analysis using a Canto II & Calibur flow cytometer (BD Biosciences, USA). Cells were stained for 30 min at 4 °C with anti-mouse antibodies, including FITC-anti-CD11c, E-Fluor@450-anti MHC class II, PE-anti-CD80 or PE-anti-CD86, and APC-anti-CCR9 (eBioscience). After staining, the cells were washed twice with PBS, and the expression of MHCII, CD80, CD86, and CCR9 on CD11c+ DCs was determined by flow cytometry. For RA dose optimization, BMDCs were incubated with different RA loading nanovaccines (0.5%, 0.75%, or 1%) for 24 h. Post-incubation, the cells were harvested for analyzing the expression of the costimulatory molecule CD86 via flow cytometry, and the supernatant was collected for IL-10 cytokine concentration analysis using ELISA.

Nanovaccines Trafficking Assay In Vivo: Cy5.5-labeled VP1 protein (50 μg) or equivalent amounts of Cy5.5-labeled nanovaccines (NM-VP1$^{T/B}$ or RA@NM-VP1$^{T/B}$) were subcutaneously administered to Balb/c mice ($n = 3$) with PBS serving as control. The distribution of the nanovaccines was monitored at predetermined intervals using the PerkinElmer IVIS spectrum system (ex: 673 nm; em: 692 nm, Massachusetts, USA). Twenty-four hours post-administration, the mice were sacrificed, and the draining lymph nodes were isolated. These lymph nodes were then analyzed in vitro using the same in vivo imaging system. For further analysis, freshly isolated lymph nodes were embedded in OCT (optimal cutting temperature) compound, sectioned, and stained with Hoechst 33 342 (Beyotime, China). Images of these sections were captured using a confocal laser scanning microscope (Nikon, Japan), and fluorescence intensity was quantified using Living Image 4.0 software.

DC Maturation in Draining Lymph Nodes: Balb/c mice ($n = 3$) were subcutaneously vaccinated at the base of their tails with different vaccine formulations, each containing 25 μg of antigen in 100 μL PBS per mouse. The draining lymph nodes were harvested and processed into single-cell suspensions after 48 h post-administration. The expression levels of MHC II, CD80, CD86, and CCR9 on CD11c+ DCs were then assessed using a flow cytometer (BD Biosciences, FACS Canto II) and analyzed with the FlowJo software (version 10.0). Additionally, MLNs were collected 48 h after vaccination to assess the migration of CD103+ DCs. Recognizing that CD103+CD11b+ DCs represent a significant migratory DC subset, single-cell suspensions from the MLNs were stained with FITC-anti-CD11c, PE-anti-mouse CD103, and Alexa Fluor 647-anti-CD11b antibodies. These samples were incubated for 40 min in the dark to determine the percentage of CD103+ CD11b+ DCs present in the MLNs.

Animal Immunization and Virus Challenge: Male BALB/c mice aged 6–8 weeks were randomly allocated into six groups, with five animals per group. They were immunized three times at two-week intervals (day 0, 14, and 28) at the base of their tails with 100 μL of various vaccine formulations, each containing 25 μg of antigen (Table S2, Supporting Information). Blood samples were collected seven days (day 35) following the final injection. Serum was then separated via centrifugation and stored at −70 °C until further use. Additionally, intestinal sections were processed into smaller pieces and ground to extract gastrointestinal wash for antigen specific IgA detection. One week after the last immunization, the mice were intraperitoneally challenged with a 3 × 50% lethal dose (3LD50) of CVB3 (day 35), and myocarditis assessments were conducted seven days post-infection (day 42). For survival analysis, the mice were challenged with a 5LD50 lethal dose of CVB3, and survival was monitored through the following 21 days.

CVB3-Specific Immune Responses: Serum and gastrointestinal wash samples from immunized mice were analyzed using ELISA to quantify levels of antigen-specific antibodies, including total IgG, IgG1, IgG2a, and IgA. For the detection of IgG titers, serum samples were serially diluted two-fold in 0.1% PBS-T containing 0.1% BSA. IgG1 and IgG2a were detected using a 1:40 dilution. Briefly, 96-well microtiter plates were coated overnight at 4 °C with 100 μL of a 10 μg mL^{-1} recombinant VP1 solution. Plates were then blocked with 5% non-fat milk in PBS, followed by the addition of either serum or intestinal lavage fluid, which were incubated at 37 °C for 2 h. After three washes, HRP-conjugated goat anti-mouse IgG, IgG1, IgG2a, or IgA antibodies (Sigma, USA, diluted 1:5000) were added and incubated for another 2 h at 37 °C. The reaction was developed using TMB substrate and stopped after 20 min at room temperature with 50 μL of 2 M sulfuric acid. Absorbance was measured at 450 nm using a microplate reader (Thermo Scientific, USA). All samples were tested in duplicate. The avidity of serum IgG was assessed using a modified ELISA with a urea-elution step.[55] Serum samples with a 1:40 dilution were tested in duplicate plates. After sample incubation, 6 M urea (Sigma) was added to one of the plates and incubated for 10 min. The results were expressed as avidity index that was calculated as the ratio of absorbance values from urea-treated plates to untreated plates. For neutralization analysis, serum samples were serially diluted two-fold from 1:2 to 1:128 and mixed with 100 TCID50/0.1 mL (median tissue culture infective dose) of CVB3, then incubated for 1 h at 37 °C. The mixtures were added to HeLa cells (2×10^4 cells per well) in 96-well plates and incubated at 37 °C in 5% CO2. After 72 h, the cytopathic effect (CPE) of CVB3 on the HeLa cells was observed using an inverted light microscope (Nikon Eclipse Ti2-E, Tokyo, Japan). Cell viability was assessed using a CCK-8 assay. Serum dilutions were tested in triplicate, and neutralization titers were calculated as the highest dilution that protected the cells from CPE.

Cytokine Measurement: Single-cell suspensions of splenocytes were prepared from the spleens of immunized mice. Specifically, spleens were harvested seven days after the last immunization, mechanically dissociated through a 70 μm cell strainer in ice-cold PBS and centrifuged at 300 g for 5 min. RBCs were lysed using ACK lysing buffer. The isolated splenocytes were then seeded at a density of 1×10^6 cells per well in 24-well culture plates (Corning, NY, USA) and cultured in 1 mL of medium containing 10 μg of each antigen. After 72 h of incubation, the supernatants from the cultures were collected and stored at −20 °C until analysis. The levels of interleukins (IL-4, IL-6), TNF-α, and IFN-γ were quantified using ELISA.

Splenocyte Proliferation and CTL Response Assays: The BeyoClick EdU-488 Cell Proliferation Assay Kit (Beyotime, China) was employed for conducting splenocyte proliferation assays as per the manufacturer's guidelines. Briefly, splenocytes were stimulated in vitro with 10 μg mL^{-1} VP1 protein for 72 h and subsequently incubated with 10 μM EdU for 2 h. Cells were then fixed in 4% formaldehyde and permeabilized with 0.3% Triton X-100. Following a PBS wash, cells were stained with the Click EdU Alexa Fluor 488 reaction mixture in the dark at room temperature for 30 min. Cell proliferation was subsequently assessed using flow cytometry (BD Biosciences, FACS Canto II, USA). To assess CVB3-specific CTL responses, a LDH cytotoxicity assay kit (Beyotime, China) was used as previously described.[56] Splenocytes were co-cultured with 10 μg mL^{-1} VP1 protein for 72 h to serve as effector cells. Autologous SP2/0 cells stably transfected with the plasmid pcDNA3.1-vp1 were used as target cells. In brief, effector and target cells were mixed in U-bottom 96-well plates at an effector to target (E/T) ratio of 50:1, with 1×10^4 target cells added per well. After a 6 h incubation at 37 °C, 50 μL of supernatant from each well was transferred to a corresponding well on a 96-well plate. Reaction mixture (50 μL) was added to each well and incubated for 30 min at room temperature. Absorbance was measured at 450 nm to determine cytotoxicity. CTL cytotoxicity percentage was calculated as follows:

$$\text{Cytotoxicity (\%)} = [(\text{effector and target cell mix-effector cell control}) - \text{low control}]/(\text{high control-low control})] \times 100\% \quad (2)$$

where "low control" represents the LDH activity from untreated normal cells (spontaneous release) and "high control" denotes LDH activity from lysed cells (maximum release), provided as the positive control in the LDH assay kits.

Evaluation of CVB3-Induced Myocarditis: Seven days following a CVB3 challenge (3LD50), cardiac function was evaluated using a high-resolution ultrasound imaging system (Vevo2100, Visual Sonics, Toronto, Canada) with a 30-MHz microscan transducer. Echocardiographic assessments of LVEF and LVFS were conducted as per the operator's manual. Subsequently, hearts were collected for histopathological examination using hematoxylin and eosin (H&E) staining. Inflammation percentages were calculated using the formula: [(number of intersections on the myocytes with inflammatory cells)/(total number of intersections on the myocytes with and without inflammatory cells)] × 100%. Histopathological changes were independently scored in a blinded manner by two investigators.

For viral titers, hearts were harvested seven days post-infection, homogenized, and centrifuged at 5000 g for 10 min to obtain tissue supernatants. HeLa cells were seeded in 96-well plates at a density of 1×10^4 cells per well and cultured until they reached 80–90% confluence. Various dilutions of the tissue supernatant (ranging from 10^{-1} to 10^{-6}) were added to the plates in 8 replicates. Untreated cells were used as negative controls, and cells infected with 100 TCID50 per 100 µL of virus served as positive controls. Diseased wells were identified by the presence of cell shrinkage and reduced light transmittance. The viral load in myocardial tissue was quantified by determining the TCID50 using the Reed-Muench method.

Statistical Analysis: The data were presented as mean ± standard deviations (SD). Statistical analyses were performed using GraphPad Prism version 9.0 software (San Diego, CA, USA). Comparisons between two groups were conducted using an unpaired, two-tailed Student's t-test. For comparisons among multiple groups, one-way ANOVA followed by Tukey's multiple comparison test was utilized. Levels of statistical significance are denoted as follows: $*p < 0.05$, $**p < 0.01$, $***p < 0.001$, and "ns" indicating no significant difference.

Supporting Information

Supporting Information is available from the Wiley Online Library or from the author.

Acknowledgements

This study was supported by the National Nature Science Foundation of China (No. 31771003) and the Priority Academic Program Development of Jiangsu Higher Education Institutions (PAPD). G.C. is supported by the Alzheimer's Association Research Grant, Olle Engkvists Stiftelse, the Petrus and Augusta Hedlunds Stiftelse, Åke Wibergs stiftelse, the Swedish Alzheimer foundation, the Åhlén Stiftelsens, Karolinska Institutet Research Foundation Grant, the Stiftelsen för Gamla Tjänarinnor, the Stiftelsen Sigurd och Elsa Goljes Minne, the Loo and Hans Osterman Foundation, Geriatric Diseases Foundation at Karolinska Institutet, the Gun and Bertil Stohne's Foundation and the Magnus Bergvall foundation. The authors thank Professor Jan Johansson for the support and constructive advice.

Conflict of Interest

The authors declare no conflict of interest.

Author Contributions

X.Q., G.W., and Y.L. contributed equally to this work. X.Q. and G.W. performed experiments. X.Q., Y.L., and G.C. analyzed data. X.Q., S.X., and G.C. conceived and supervised this study. X.Q. and G.C. wrote the manuscript. All authors commented on the manuscript.

Data Availability Statement

The data that support the findings of this study are available from the corresponding author upon reasonable request.

Keywords

Coxsackievirus B3, enterovirus, minor ampullate silk protein, nanoparticles, systemic and mucosal immune responses

Received: May 3, 2024
Revised: June 16, 2024
Published online:

[1] S. Plotkin, *Proc. Natl. Acad. Sci. USA* **2014**, *111*, 12283.
[2] A. Gutjahr, G. Tiraby, E. Perouzel, B. Verrier, S. Paul, *Trends Immunol.* **2016**, *37*, 573.
[3] B. Pulendran, R. Ahmed, *Nat. Immunol.* **2011**, *12*, 509.
[4] D. Baxter, *Occup. Med. (Lond)* **2007**, *57*, 552.
[5] K. Stratton, A. Ford, E. Rusch, E. W. Clayton, *Adverse Effects of Vaccines: Evidence and Causality*, National Academies Press, Washington (DC) **2011**.
[6] A. Vartak, S. J. Sucheck, *Vaccines (Basel)* **2016**, *4*, 12.
[7] X. Zhong, G. Du, X. Wang, Y. Ou, H. Wang, Y. Zhu, X. Hao, Z. Xie, Y. Zhang, T. Gong, Z. Zhang, X. Sun, *Small* **2022**, *18*, 2105530.
[8] S. I. Hammerschmidt, M. Friedrichsen, J. Boelter, M. Lyszkiewicz, E. Kremmer, O. Pabst, R. Förster, *J. Clin. Invest.* **2011**, *121*, 3051.
[9] D. R. Frederick, J. A. Goggins, L. M. Sabbagh, L. C. Freytag, J. D. Clements, J. B. McLachlan, *Mucosal Immunol.* **2018**, *11*, 549.
[10] D. Christensen, L. Bøllehuus Hansen, R. Leboux, W. Jiskoot, J. P. Christensen, P. Andersen, J. Dietrich, *ACS Nano* **2019**, *13*, 1116.
[11] Y. Xia, J. Wu, Y. Du, C. Miao, Z. Su, G. Ma, *Adv. Mater.* **2018**, *30*, 1801067.
[12] D. Fairweather, K. A. Stafford, Y. K. Sung, *Curr. Opin. Rheumatol.* **2012**, *24*, 401.
[13] A. Pollack, A. R. Kontorovich, V. Fuster, G. W. Dec, *Nat. Rev. Cardiol.* **2015**, *12*, 670.
[14] J. A. Towbin, A. M. Lowe, S. D. Colan, L. A. Sleeper, E. J. Orav, S. Clunie, J. Messere, G. F. Cox, P. R. Lurie, D. Hsu, C. Canter, J. D. Wilkinson, S. E. Lipshultz, *JAMA, J. Am. Med. Assoc.* **2006**, *296*, 1867.
[15] N. P. Tavakoli, H. Wang, S. Nattanmai, M. Dupuis, H. Fusco, R. Hull, *J. Clin. Virol.* **2008**, *43*, 207.
[16] J. Hong, B. Kang, S. Yeo, Y. Jee, J. H. Park, *J. Vet. Sci.* **2017**, *18*, 457.
[17] S. Huber, A. I. Ramsingh, *Viral Immunol.* **2004**, *17*, 358.
[18] Q. Mao, Y. Wang, L. Bian, M. Xu, Z. Liang, *Emerg. Microbes Infect.* **2016**, *5*, 1.
[19] H. Hyöty, F. Leon, M. Knip, *Expert Rev. Vaccines* **2018**, *17*, 1071.
[20] S. J. Richardson, N. G. Morgan, *Curr. Opin. Pharmacol.* **2018**, *43*, 11.
[21] N. Principi, M. G. Berioli, S. Bianchini, S. Esposito, *J Clin. Virol.* **2017**, *96*, 26.
[22] J. L. Dunne, S. J. Richardson, M. A. Atkinson, M. E. Craig, K. Dahl-Jørgensen, M. Flodström-Tullberg, H. Hyöty, R. A. Insel, Å. Lernmark, R. E. Lloyd, N. G. Morgan, A. Pugliese, *Diabetologia* **2019**, *62*, 744.
[23] O. H. Laitinen, H. Honkanen, O. Pakkanen, S. Oikarinen, M. M. Hankaniemi, H. Huhtala, T. Ruokoranta, V. Lecouturier, P. André, R. Harju, S. M. Virtanen, J. Lehtonen, J. W. Almond, T. Simell, O. Simell, J. Ilonen, R. Veijola, M. Knip, H. Hyöty, *Diabetes* **2014**, *63*, 446.
[24] K. Mone, N. Lasrado, M. Sur, J. Reddy, *Vaccines (Basel)* **2023**, *11*, 274.
[25] G. Liu, M. Zhu, X. Zhao, G. Nie, *Adv. Drug Delivery Rev.* **2021**, *176*, 113889.
[26] C. Zhang, Y. Zhang, Y. Li, J. Lu, S. Xiong, Y. Yue, *Virology* **2023**, *579*, 46.

[27] V. Asgari, A. Landarani-Isfahani, H. Salehi, N. Amirpour, B. Hashemibeni, M. Kazemi, H. Bahramian, *J. Mol. Neurosci.* **2020**, *70*, 1836.
[28] T. Cai, H. Liu, S. Zhang, J. Hu, L. Zhang, *J Nanobiotechnology* **2021**, *19*, 389.
[29] Y. Du, T. Song, J. Wu, X. D. Gao, G. Ma, Y. Liu, Y. Xia, *Biomaterials* **2022**, *280*, 121313.
[30] L. Meinel, S. Hofmann, V. Karageorgiou, C. Kirker-Head, J. McCool, G. Gronowicz, L. Zichner, R. Langer, G. Vunjak-Novakovic, D. L. Kaplan, *Biomaterials* **2005**, *26*, 147.
[31] F. Vollrath, P. Barth, A. Basedow, W. Engstrom, H. List, *In vivo* **2002**, *16*, 229.
[32] M. M. Moisenovich, O. L. Pustovalova, A. Y. Arhipova, T. V. Vasiljeva, O. S. Sokolova, V. G. Bogush, V. G. Debabov, V. I. Sevastianov, M. P. Kirpichnikov, I. I. Agapov, *J. Biomed. Mater. Res. A* **2011**, *96*, 125.
[33] C. Fredriksson, M. Hedhammar, R. Feinstein, K. Nordling, G. Kratz, J. Johansson, F. Huss, A. Rising, *Materials* **2009**, *2*, 1908.
[34] M. Hofer, G. Winter, J. Myschik, *Biomaterials* **2012**, *33*, 1554.
[35] H. Yu, G. Chen, L. Li, G. Wei, Y. Li, S. Xiong, X. Qi, *MedComm* **2024**, *5*, 573.
[36] A. Henke, R. Zell, A. Stelzner, *Antiviral Res.* **2001**, *49*, 49.
[37] N. Lasrado, A. Gangaplara, R. Arumugam, C. Massilamany, S. Pokal, Y. Zhou, S. H. Xiang, D. Steffen, J. Reddy, *Viruses* **2020**, *12*, 347.
[38] H. Zhang, L. Zeng, Q. Liu, G. Jin, J. Zhang, Z. Li, Y. Xu, H. Tian, S. Deng, Q. Shi, X. Huang, *PLoS Pathog.* **2021**, *17*, 1008992.
[39] N. Lasrado, A. Gangaplara, C. Massilamany, R. Arumugam, A. Shelbourn, M. T. Rasquinha, R. H. Basavalingappa, G. Delhon, S. H. Xiang, A. K. Pattnaik, D. Steffen, J. Reddy, *Sci. Rep.* **2021**, *11*, 12432.
[40] C. M. Haarmann, P. L. Schwimmbeck, T. Mertens, H. P. Schultheiss, B. E. Strauer, *Virology* **1994**, *200*, 381.
[41] H. Cai, G. Chen, H. Yu, Y. Tang, S. Xiong, X. Qi, *BMC Biotechnol.* **2020**, *20*, 37.
[42] U. K. Slotta, S. Rammensee, S. Gorb, T. Scheibel, *Angew. Chem., Int. Ed.* **2008**, *47*, 4592.
[43] A. Lammel, M. Schwab, U. Slotta, G. Winter, T. Scheibel, *ChemSusChem* **2008**, *1*, 413.
[44] D. Fairweather, S. Frisancho-Kiss, S. A. Yusung, M. A. Barrett, S. E. Davis, R. A. Steele, S. J. Gatewood, N. R. Rose, *J. Immunol.* **2005**, *174*, 261.
[45] C. Wang, G. Fung, H. Deng, J. Jagdeo, Y. Mohamud, Y. C. Xue, E. Jan, J. A. Hirota, H. Luo, *FASEB J.* **2019**, *33*, 942.
[46] M. Humenik, K. Pawar, T. Scheibel, *Adv. Exp. Med. Biol.* **2019**, *1174*, 187.
[47] M. Lucke, I. Mottas, T. Herbst, C. Hotz, L. Römer, M. Schierling, H. M. Herold, U. Slotta, T. Spinetti, T. Scheibel, G. Winter, C. Bourquin, J. Engert, *Biomaterials* **2018**, *172*, 105.
[48] K. Schacht, T. Scheibel, *Curr. Opin. Biotechnol.* **2014**, *29*, 62.
[49] S. Salehi, K. Koeck, T. Scheibel, *Molecules* **2020**, *25*, 737.
[50] L. Lattanzi, M. Federico, *Vaccine* **2012**, *30*, 7229.
[51] Y. Waeckerle-Men, E. U. Allmen, B. Gander, E. Scandella, E. Schlosser, G. Schmidtke, H. P. Merkle, M. Groettrup, *Vaccine* **2006**, *24*, 1847.
[52] K. Sehgal, K. M. Dhodapkar, M. V. Dhodapkar, *Immunol. Lett.* **2014**, *162*, 59.
[53] X. Qi, Q. Lu, J. Hu, S. Xiong, *Microb. Cell Fact.* **2019**, *18*, 66.
[54] X. Qi, Y. Sun, S. Xiong, *Microb. Cell Fact.* **2015**, *14*, 24.
[55] A. V. Capozzo, K. Ramírez, J. M. Polo, J. Ulmer, E. M. Barry, M. M. Levine, M. F. Pasetti, *J. Immunol.* **2006**, *176*, 5671.
[56] Y. Gao, Y. Yue, S. Xiong, *Front. Immunol.* **2021**, *12*, 666594.